Earth and Planetary Science Letters 605 (2023) 118032

Contents lists available at ScienceDirect

Earth and Planetary Science Letters

journal homepage: www.elsevier.com/locate/epsl

Nitrogen and carbon fractionation in planetary magma oceans and origin of the superchondritic C/N ratio in the bulk silicate Earth

Yuan Li [a,b,*], Michael Wiedenbeck [c], Brian Monteleone [e], Rajdeep Dasgupta [d], Gelu Costin [d], Zenghao Gao [a,b], Wenhua Lu [a,b]

[a] State Key Laboratory of Isotope Geochemistry, Guangzhou Institute of Geochemistry, Chinese Academy of Sciences, Guangzhou 510640, China
[b] CAS Center for Excellence in Deep Earth Science, Guangzhou, 510640, China
[c] Helmholtz Zentrum Potsdam, Deutsches GeoForschungZentrum, GFZ, Telegrafenberg, 14473 Potsdam, Germany
[d] Department of Geology and Geophysics, Woods Hole Oceanographic Institution, Woods Hole, MA 02543, USA
[e] Department of Earth, Environmental, and Planetary Sciences, Rice University, 6100 Main Street, MS 126, Houston, TX 77005, USA

ARTICLE INFO

Article history:
Received 6 November 2022
Received in revised form 21 January 2023
Accepted 23 January 2023
Available online 3 February 2023
Editor: F. Moynier

Keywords:
nitrogen and carbon
solubility and partitioning
degassing
core formation
magma ocean

ABSTRACT

Volatiles are important for planetary geodynamics, climate, and habitability. The C/N ratio of the bulk silicate Earth (BSE) is superchondritic, which provides a useful tool for understanding the origin of Earth's volatiles. The Earth accreted largely from differentiated planetesimals and embryos, and the fate of nitrogen and carbon in magma oceans (MOs) of such rocky bodies is key in shaping the BSE's C/N ratio. Here we present experiments performed at 0.3–3 GPa and 1400–1600 °C to determine both the solubility and partitioning of nitrogen and carbon between Fe-rich metallic and silicate melts at graphite-saturation and the saturation of N_2-rich gas. The quenched samples were analyzed by electron microprobe, secondary ion mass spectrometry, and Raman spectroscopy for their N–C–H–O contents and speciation. Our results show that the C/N solubility ratios of the silicate melts (ppm/ppm by wt.) are a multi-function of pressure, temperature, silicate melt composition, and mainly oxygen fugacity (fO_2), and increase from 0.01 to 1.6 with increasing fO_2 from IW-3.7 to IW+0.4 (IW refers to the iron–wüstite buffer). Raman spectra and theoretical considerations reveal that the main species in silicate melts are N_2, N^{3-}, and N–H in the case of nitrogen, and CO, CO_3^{2-}, and C–H in the case of carbon. Nitrogen and carbon may also form complex species, which, however, could not be identified presently. The metal/silicate partition coefficients of nitrogen and carbon $D_{N,C}^{metal/silicate}$ are 1–114 and 34–3050, respectively. The $D_C^{metal/silicate}/D_N^{metal/silicate}$ ratios are 1.5–1100, which decrease with increasing pressure, fO_2, and the water content in silicate melts. Our results imply that N–C fractionation could occur during core-formation and silicate MO degassing. For a rocky body starting with a chondritic C/N ratio, core-formation would result in a superchondritic C/N ratio in its core if that rocky body is S- and Si-poor. However, a superchondritic C/N ratio can also be achieved in the silicate mantle through C-saturation coupled with preferential nitrogen degassing and loss into space, if the rocky body is oxidized and has a S-rich core, or is reduced and has a Si-rich core. Both Earth's accretion of planetesimals and embryos with cores as the major nitrogen and carbon reservoirs, and Earth's disequilibrium accretion of C-saturated embryos through core–core merging, could have helped establish the BSE's superchondritic C/N ratio. During Earth's accretion of the last few giant impactors, multiple episodes of MO degassing and erosion-induced atmospheric loss would have also favored the formation of a superchondritic C/N ratio in the BSE, due to the oxidized nature of Earth's surface MO (fO_2 > IW) and the preferential loss of nitrogen into space. Finally, we emphasize that oxidization of emulsified planetesimal cores in Earth's upper mantle during its final accretion stages could have further helped establish the BSE's superchondritic C/N ratio. Accordingly, the BSE's superchondritic C/N ratio may be an outcome of combined processes operating both on the accreted planetesimals and embryos and on the proto-Earth itself.

1. Introduction

The origin of Earth's volatiles remains an active topic of debate and research (Dalou et al., 2017; Dasgupta et al., 2013; Grewal et

* Corresponding author at: State Key Laboratory of Isotope Geochemistry, Guangzhou Institute of Geochemistry, Chinese Academy of Sciences, Guangzhou 510640, China.
E-mail address: Yuan.Li@gig.ac.cn (Y. Li).

https://doi.org/10.1016/j.epsl.2023.118032
0012-821X/

al., 2019b; Hirschmann, 2016; Li et al., 2016a; Marty, 2012; Shi et al., 2022; Wang and Becker, 2013). The model based on chondritic Se, Te, and S ratios and Se isotopic composition of the bulk silicate Earth (BSE) argued that the Earth accreted dry and gained its volatiles from an undifferentiated "late veneer" of carbonaceous chondrite (CC)-like materials (Albarede, 2009; Varas-Reus et al., 2019; Wang and Becker, 2013). However, the BSE has a superchondritic C/N ratio, which means that the BSE's C/N ratio is higher than that in CI chondrites due to the BSE's depletion of N (Dasgupta and Grewal, 2019; Hirschmann, 2016; Marty, 2012). This observation together with the Ru isotopic evidence for an inner solar system origin of the late veneer (Fischer-Godde and Kleine, 2017) excludes the addition of unprocessed late chondritic impactors as a major source of Earth's volatiles. The Earth may have thus acquired its volatiles during the main accretion phase, as indicated by the BSE's isotopic compositions of both volatile and refractory siderophile elements (Budde et al., 2019; Labidi et al., 2013; Schönbächler et al., 2010; Shi et al., 2022). This model implies that volatiles must have participated in Earth's core–mantle segregation in a magma ocean (MO), where the processing of volatiles could have defined the BSE's volatile budget and ratios (Dalou et al., 2017; Duncan et al., 2017; Grewal et al., 2019a,b; Li et al., 2015a, 2016a,b). The inner Solar System planets including Earth formed largely from accretions of numerous planetesimals and Moon to Mars-sized embryos that had already differentiated into a metallic core and silicate mantle (Elkins-Tanton, 2012; Greenwood et al., 2005; Rubie et al., 2015). Accordingly, the quantity and distribution of volatiles in such differentiated bodies must have also played an important role in shaping Earth's volatile budget and ratios (Grewal et al., 2021b, 2019b; Li et al., 2016a; Tsuno et al., 2018). In addition, the collisions experienced by the protoplanets could lead to catastrophic loss of material, such as a proto-atmosphere, and Earth's volatile budget and ratios could be influenced by preferential erosion of chemically distinct layers (Kegerreis et al., 2020).

Ratios of volatile elements are powerful tools for understanding Earth's accretion of volatiles, as they can track the relative fractionation through important accretion and differentiation processes (Chen and Jacobson, 2022; Dasgupta and Grewal, 2019; Grewal et al., 2019b, 2022; Hirschmann, 2016; Li et al., 2016a; Marty et al., 2020). The fate of volatiles in a planetary MO is dictated by their dissolution and partitioning among core, mantle, and atmosphere (Chi et al., 2014; Elkins-Tanton, 2012; Grewal et al., 2019b; Hirschmann, 2016; Li et al., 2015a; Sarafian et al., 2017). Therefore, the solubility and partitioning of N and C in Fe-rich metallic and silicate melts at conditions relevant for MOs of planetesimals and embryos should be investigated in order to understand the origin of the BSE's superchondritic C/N ratio in particular, and the origin of Earth's volatiles in general. Previous studies have determined the solubility and partitioning of C between metallic and silicate melts at 1–71 GPa,1573–5200 K, and oxygen fugacity (fO_2) of IW-6 to IW+1 (Blanchard et al., 2022; Chi et al., 2014; Dasgupta et al., 2013; Fichtner et al., 2021; Fischer et al., 2020; Grewal et al., 2021a; Li et al., 2015a, 2016a; Malavergne et al., 2019). The main results are that the metal/silicate partition coefficients of C ($D_C^{metal/silicate}$) are ~10–10^5, and the C-solubility in silicate melt at graphite-saturation ($S_C^{silicate}$) is ~10–5700 ppm by wt. Both $D_C^{metal/silicate}$ and $S_C^{silicate}$ are functions of P–T, fO_2, and metallic and silicate melt compositions. Several other studies have determined $D_N^{metal/silicate}$ at 1–26 GPa, 1673–3437 K, and fO_2 of IW-7 to IW, which are ~0.01–100 and are controlled strongly by fO_2 (Dalou et al., 2017; Grewal et al., 2019a, 2021b; Jackson et al., 2021; Li et al., 2016b; Roskosz et al., 2013; Shi et al., 2022; Speelmanns et al., 2019). The N-solubility in silicate melt at the saturation of N_2-rich gas ($S_N^{silicate}$) has been determined at 1 bar to 8 GPa, which shows a strong dependence on fO_2, pressure, and silicate melt composition (Bernadou et al., 2021; Boulliung et al., 2020; Dasgupta et al., 2022; Gao et al., 2022; Keppler et al., 2022; Libourel et al., 2003). However, only two studies have simultaneously determined $D_C^{metal/silicate}$ and $D_N^{metal/silicate}$ at graphite-saturated but N_2-undersaturated conditions; these have shown that $D_C^{metal/silicate}$ are significantly higher than $D_N^{metal/silicate}$, except that the metallic melts are highly S-rich (Dalou et al., 2017; Grewal et al., 2019b).

The relative behavior of N and C during planetesimal/embryo core–mantle segregation and its influence on the C/N ratio in the BSE were evaluated by Grewal et al. (2019b). However, the effect of degassing on N–C fractionation in planetary MOs and its influence on the BSE's C/N ratio have not yet been investigated, although volatile-loss was observed to be universal for differentiated asteroids (Collinet and Grove, 2020; Elkins-Tanton, 2012; Sarafian et al., 2017). Here we perform laboratory experiments to simultaneously determine $S_{N,C}^{silicate}$ and $D_{N,C}^{metal/silicate}$ at MO conditions (0.3–3 GPa, 1400–1600 °C, and ΔIW = −3.7 to 0.4) relevant for planetesimals and embryos. These results are then used to understand N–C fractionation during planetary core–mantle–atmosphere differentiation and the possible origin of the BSE's superchondritic C/N ratio.

2. Methods

2.1. Starting materials

Our starting materials were composed of synthetic silicates, metallic Si and Ni, Fe_7N_3, and Si_3N_4. Major element compositions of the synthetic silicates were similar to those of lunar basalt, Martian basalt, or mid-ocean ridge basalt (Table S1). All synthetic silicates were prepared from high-purity oxides and carbonates as described in Li et al. (2017). The silicate powders were reduced and decarbonated at 1000 °C and fO_2 of ~IW+2 for 24 h using a CO–CO_2 gas mixing furnace. The starting materials were then stored in a vacuum oven at 100 °C for >24 h before loading into graphite-lined $Pt_{95}Rh_{05}$ capsules. In each sample capsule, ~50 wt% silicate and ~50 wt% Fe_7N_3 ± Ni ± Si ± Si_3N_4 powder were added. The addition of ~50 wt% Fe_7N_3 was to ensure the presence of an Fe-rich metallic phase and also to assure the saturation of N_2-rich gas. The addition of Ni, Si, or Si_3N_4 was used to vary the composition of the metallic melt and the sample fO_2. In one experiment, only ~95 wt% silicate and ~5 wt% NH_4NO_3 were loaded into the sample capsule to measure $S_N^{silicate}$ in a relatively oxidized silicate melt.

2.2. High-pressure experiments

High-pressure experiments were designed to investigate the effects that P–T, fO_2, and the compositions of the metallic and silicate melts have on $S_{N,C}^{silicate}$ and $D_{N,C}^{metal/silicate}$. The experiments were performed at 1–3 GPa and 1400–1600 °C or at 0.3–0.6 GPa and 1400 °C in an end-loaded, solid media piston cylinder apparatus, using 1/2-inch or 3/4-inch diameter talc-Pyrex assemblies with graphite heaters, respectively. Pressure was calibrated against the quartz-coesite and kyanite-sillimanite transitions, and friction corrections of 20% and 18% were applied for the 1/2-inch and 3/4-inch assemblies, respectively. The pressure uncertainty was estimated to be better than 0.1 GPa. The D-type ($W_{97}Re_{03}$–$W_{75}Re_{25}$) and S-type (Pt–$Pt_{90}Rh_{10}$) thermocouples were used for the experiments at 1500–1600 °C and 1400 °C, respectively. The experimental temperature was controlled to ±2 °C and was accurate to ±10 °C. All experiments were terminated by switching off the electric power supplied to the graphite heaters. After being immersed in water, a hole was drilled in the recovered sample capsules using a sharp needle in order to check whether the samples were saturated with N_2-rich gas. Those samples that were saturated with N_2-rich gas

were prepared for the analyses using electron microprobe, secondary ion mass spectrometry (SIMS), and Raman spectroscopy.

2.3. Analyses

We analyzed our samples by using electron microprobe for major elements, SIMS for C–N–H contents in silicate melts, and Raman spectroscopy for C–N–H species in silicate melts. A brief description of the analytical conditions is provided below, with further details given in the Supplementary Materials. Major element compositions of the quenched metallic and silicate melts were analyzed using a JEOL JXA8530F Hyperprobe at Rice University, using the same procedures and standardization as described previously (Grewal et al., 2019a,b). The silicate phases were analyzed using carbon-coated samples, while the metallic phases were analyzed using an aluminum-coating. Synthetic iron nitride (Fe_3N) and iron carbide (Fe_3C) were used as standard for measuring N and C in the metallic melts, and the detection limits were ~500 ppm and ~0.2 wt%, respectively.

The bulk C and water content in our silicate glasses were determined using a SIMS-1280 at Woods Hole Oceanographic Institution, using the same procedures and standardization as described previously (Grewal et al., 2019b; Li et al., 2017, 2016a). Calibration for CO_2 and water were obtained by replicate measurements of $^{12}C/^{30}Si$ and $^{1}H^{16}O/^{30}Si$ ratios in standard glasses with basaltic compositions (Fig. S1a, b). About 4–6 spots were analyzed for each sample glass and each spot included 10 analytical cycles. During the whole analytical session, one or two analyses were performed on the standard glass after each three analyses on the sample for checking the possible deviation and accuracy. The uncertainties of our measured water and carbon contents are better than 6%. The N content in the silicate glasses was determined using SIMS-1280HR at GFZ, Potsdam. Our calibration curve (Fig. S1c) was based on a suite of 6 basaltic glass materials which have previously been characterized for their absolute N contents (Füri et al., 2018); these included a blank material nominally containing 0 ppm N and the highest concentration material with 18400 ppm N. Our N concentration values for the silicate glasses in the range of a few hundred to 10000 ppm N are reliable to 5% or better. At lower concentrations data quality was limited by counting statistics.

Raman spectra of the silicate glasses were collected from 200 to 4500 cm^{-1} with acquisition time of 2 × 300 s for each range, in order to detect N–C–H–O species with low concentrations. The 514.5 nm line of an Ar^+ ion laser with an output power 0.1 W was used for excitation. Micro-Raman spectra were recorded in backscattering geometry using a Horiba LabRAM HR UV spectrometer with CCD detector, 1800 mm^{-1} grating, 50× objective, and confocal mode. A confocal pinhole of 100 μm was used, which limits spectral resolution to 3.5 cm^{-1}.

2.4. Oxygen fugacity calculations

The fO_2 of our experiments was calculated from the equilibrium of Fe-rich metallic and FeO-bearing silicate melts (Grewal et al., 2019a; Li et al., 2016a):

$$\mathrm{FeO\,(silicate)} = \mathrm{Fe\,(metal)} + 1/2\mathrm{O_2} \quad (1)$$

from which the fO_2 relative to the IW buffer at any given P–T can be defined as:

$$\Delta\mathrm{IW} = 2\log(\alpha_{\mathrm{FeO}}/\alpha_{\mathrm{Fe}}) = 2\log[(x_{\mathrm{FeO}}\cdot\gamma_{\mathrm{FeO}})/(x_{\mathrm{Fe}}\cdot\gamma_{\mathrm{Fe}})] \quad (2)$$

where α_{FeO} and α_{Fe} represent the activity of FeO in the silicate melt and the activity of Fe in the metallic melt, respectively; x_{FeO} and x_{Fe} are molar fractions of FeO in the silicate melt and Fe in the metallic melt, respectively; γ_{FeO} and γ_{Fe} are activity coefficients of FeO in the silicate melt and Fe in the metallic melt, respectively. We performed calculations of fO_2 using both ideal (ideal fO_2; the activity coefficients of FeO in the silicate melt and Fe in the metallic melt equal one) and non-ideal solution models (non-ideal fO_2). The non-ideal fO_2 calculation assumed γ_{FeO} equivalent to 1.5, and γ_{Fe} was calculated using the ε-approach (Grewal et al., 2019a; Li et al., 2016a), in which the non-ideal interactions between all components in the metallic melt are considered (Wood et al., 2013).

3. Results

All our experimental conditions and products are summarized in Table 1, with representative sample petrography shown in Fig. 1. All experiments produced blobs of metallic melts embedded in the silicate melts, except for run D-7 which started with only silicate and NH_4NO_3. The metallic melts exsolved into minor phases during quench, whereas the silicate melts were quenched into glasses. We observed different-sized vesicles distributed in the metallic and silicate melts (Fig. 1), suggesting the saturation of N_2-rich gas in our nominally anhydrous samples. The calculated non-ideal fO_2 values, which will be used hereafter, are IW+0.37 to IW-3.7, ~0.5–0.7 log units higher than the corresponding ideal fO_2 values. We believe that the fO_2 of run D-7 is close to the C–CO_2 buffer (~IW+2) as the reaction $2NH_4NO_3 + C\,(\mathrm{graphite}) = 2N_2 + 4H_2O + CO_2$ may have produced significant CO_2 in the graphite capsule.

3.1. Major element compositions

Major element compositions of the quenched metallic and silicate melts are given in Tables S2 and S3. The silicate melts had 0.8–24 wt% FeO_{tot}; the low FeO_{tot} contents were caused by the reduction of FeO_{tot} by Si in the metallic melts, whereas the high FeO_{tot} contents resulted from the partial oxidation of the metallic melts. The non-bridging oxygens to tetrahedral cations (NBO/T) ratios of the silicate melts were 0.4–1.9. The metallic melts contained ~25–75 wt% Ni and ~25–71 wt% Fe in several experiments, and 91–95 wt% Fe in other experiments. Si contents in the metallic melts were up to ~3.14 wt%. The N-solubility in the metallic melts at the saturation of N_2-rich gas (S_N^{metal}) ranged from below detection limit (~0.05 wt%) to 3 wt%; the C-solubility at graphite-saturation (S_C^{metal}) ranged from 1.5 to 5.0 wt%. Both S_N^{metal} and S_C^{metal} decrease with increasing the Ni content in the metallic melts (Fig. 2a). S_N^{metal} increases, but S_C^{metal} decreases, with increasing pressure (Fig. 2b). The S_C^{metal}/S_N^{metal} ratios decrease from ~70 down to 1 when the pressure increases from 0.3 to 3 GPa (Fig. 2c). Temperature does not considerably affect S_C^{metal} or S_N^{metal} (Fig. 2a, b). The observed Ni-dependence of S_C^{metal} and S_N^{metal} is consistent with previous studies at high pressures (Dasgupta et al., 2013; Roskosz et al., 2013), and the correlation between S_N^{metal} and pressure (Fig. 2b) also agrees with the nearly linear correlation observed at pressures below 4 GPa in a previous study (Speelmanns et al., 2018). However, the observation that S_C^{metal} decreases with increasing pressure contrasts with previous results that showed that S_C^{metal} does not change much with pressure up to 8 GPa in N-free systems (Li et al., 2016a). The difference can be explained by the expulsion of C by N in the metallic melts in this study.

3.2. The N–C–H content in silicate melts

Water, N, and C were all homogeneously distributed in the silicate melts, with variations less than 20% relative for most of our samples (Table 1). The water contents in our silicate melts ranged between 0.01–0.94 wt%. The $S_N^{silicate}$ and $S_C^{silicate}$ were 60–10800 and 14–420 ppm, respectively. The $S_C^{silicate}$ increases with increasing fO_2, whereas $S_N^{silicate}$ decreases with increasing

Table 1
Summary of experimental conditions and obtained products.

Run No.	P (GPa)	T (°C)	Run duration (min)	[a]Starting materials	Capsule	[b] log fO_2 ΔIW	[c] log fO_2 ΔIW	[d]Run products	H_2O in silicate (wt%)	1-σ	C in silicate (ppm)	1-σ	C in metal (wt%)	1-σ	N in silicate (ppm)	1-σ	N in metal (wt%)	1-σ	$D_C^{metal/silicate}$	1-σ	$D_N^{metal/silicate}$	1-σ
NS-1	1	1400	240	Fe_7N_3 + MORB	Graphite-lined $Pt_{95}Rh_{05}$	−1.33	−0.77	Metal + silicate	0.79	0.04	104	14	4.24	0.39	204	19	0.79	0.18	410	68	39	10
NS-2	1	1400	235	Fe_7N_3 + NWA	Graphite-lined $Pt_{95}Rh_{05}$	−1.20	−0.63	Metal + silicate	0.61	0.01	141	25	4.12	0.23	133	6	0.84	0.10	292	55	63	8
NS-3	1	1500	180	Fe_7N_3 + MORB	Graphite-lined $Pt_{95}Rh_{05}$	−1.41	−0.85	Metal + silicate	0.89	0.01	128	25	4.40	0.42	247	7	0.65	0.20	345	76	27	8
NS-4	1	1600	80	Fe_7N_3 + MORB	Graphite-lined $Pt_{95}Rh_{05}$	−1.38	−0.79	Metal + silicate	0.59	0.02	260	33	4.75	0.20	336	19	0.58	0.09	183	24	17	3
NS-5	1.8	1500	180	Fe_7N_3 + MORB	Graphite-lined $Pt_{95}Rh_{05}$	−1.37	−0.80	Metal + silicate	0.77	0.02	160	8	3.81	0.33	474	23	1.87	0.23	238	24	39	5
NS-6	3	1500	200	Fe_7N_3 + MORB	Graphite-lined $Pt_{95}Rh_{05}$	−1.36	−0.80	Metal + silicate	0.32	0.07	174	72	3.21	0.08	821	20	3.02	0.11	185	76	37	2
NS-7	1	1400	80	Fe_7N_3 + LTB	Graphite-lined $Pt_{95}Rh_{05}$	−1.34	−0.75	Metal + silicate	n.d.		n.d.		4.32	0.47	227	72	1.06	0.21	n.d.		47	17
NS-8	2.5	1600	90	Fe_7N_3 + LTB	Graphite-lined $Pt_{95}Rh_{05}$	−1.27	−0.68	Metal + silicate	n.d.		n.d.		4.11	0.36	188	27	2.15	0.12	n.d.		114	18
NS-9	2.5	1600	60	Fe_7N_3 + NWA	Graphite-lined $Pt_{95}Rh_{05}$	−1.25	−0.74	Metal + silicate	n.d.		n.d.		3.42	0.56	552	28	2.15	0.27	n.d.		39	5
NS-10	1	1600	80	Fe_7N_3 + LTB	Graphite-lined $Pt_{95}Rh_{05}$	n.d.	n.d.	Metal + silicate	0.67	0.01	304	10	n.d.		190	6	n.d.		n.d.		n.d.	
NS-11	1	1600	60	Fe_7N_3 + NWA	Graphite-lined $Pt_{95}Rh_{05}$	n.d.	n.d.	Metal + silicate	0.94	0.02	280	24	n.d.		227	17	n.d.		n.d.		n.d.	
NS-12	1	1400	120	Fe_7N_3 + 20%Ni + MORB	Graphite-lined $Pt_{95}Rh_{05}$	−1.25	−0.65	Metal + silicate	0.59	0.01	86	2	3.19	0.17	239	3	0.46	0.13	369	22	19	5
NS-13	1	1400	120	Fe_7N_3 + 30%Ni + NWA	Graphite-lined $Pt_{95}Rh_{05}$	−0.86	−0.24	Metal + silicate	0.61	0.01	144	9	2.63	0.51	134	12	0.28	0.10	182	37	21	8
NS-14	1	1400	300	Fe_7N_3 + 70%Ni + NWA	Graphite-lined $Pt_{95}Rh_{05}$	−0.27	0.37	Metal + silicate	0.86	0.02	183	1	0.62	0.07	114	27	0.00	0.00	34	4		
NS-15	1	1400	300	Fe_7N_3 + 3%Si + MORB	Graphite-lined $Pt_{95}Rh_{05}$	−2.20	−1.64	Metal + silicate	0.35	0.01	60	5	4.41	0.08	1081	9	0.61	0.08	736	64	6	1
NS-16	1	1400	300	Fe_7N_3 + 10%Si + MORB	Graphite-lined $Pt_{95}Rh_{05}$	−4.15	−3.65	Metal + silicate	0.71	0.04	60	1	3.45	1.51	10807	481	0.54	0.11	570	249	1	0
NS-17	0.6	1400	120	Fe_7N_3 + MORB	Graphite-lined $Pt_{95}Rh_{05}$	−1.33	−0.72	Metal + silicate	0.34	0.01	79	2	4.95	1.29	150	7	0.42	0.14	630	165	28	9
NS-18	0.3	1400	120	Fe_7N_3 + MORB	Graphite-lined $Pt_{95}Rh_{05}$	−1.35	−0.76	Metal + silicate	0.11	0.01	50	8	4.57	0.45	73	7	0.07	0.08	921	171	9	11
NS-19	2.5	1600	60	Fe_7N_3 + 3%Si + LTB	Graphite-lined $Pt_{95}Rh_{05}$	−0.82	−0.16	Metal + silicate	0.16	0.03	330	65	2.98	0.09	397	3	0.81	0.10	90	18	20	2
NS-20	2.5	1600	60	Fe_7N_3 + 40%Ni + NWA	Graphite-lined $Pt_{95}Rh_{05}$	−1.56	−0.97	Metal + silicate	0.80	0.01	422	3	4.03	0.31	335	20	2.17	0.26	96	7	65	9
D-1	0.3	1400	80	Fe_7N_3 + MORB	Graphite-lined $Pt_{95}Rh_{05}$	−1.44	−0.88	Metal + silicate	0.06	0.00	39	2	4.31	0.55	71	3	0.11	0.07	1099	151	15	10
D-2	0.3	1400	60	Fe_7N_3 + 3%Si + MORB	Graphite-lined $Pt_{95}Rh_{05}$	−2.01	−1.46	Metal + silicate	0.06	0.00	14	2	4.31	0.55	123	27	0.11	0.07	3049	532	9	6
D-3	0.3	1400	120	Fe_7N_3 + 5%Si + MORB	Graphite-lined $Pt_{95}Rh_{05}$	−1.94	−1.37	Metal + silicate	0.07	0.01	27	2	4.33	0.26	109	8	0.14	0.03	1584	169	13	3
D-5	0.3	1400	70	Fe_7N_3 + 30%Ni + MORB	Graphite-lined $Pt_{95}Rh_{05}$	−1.39	−0.78	Metal + silicate	0.12	0.01	44	5	3.27	0.99	87	1	< 500 ppm		740	242	< 6	
D-6	0.3	1400	60	Fe_7N_3 + 50%Ni + MORB	Graphite-lined $Pt_{95}Rh_{05}$	−1.18	−0.58	Metal + silicate	0.21	0.00	55	20	1.54	0.49	88	4	< 500 ppm		281	136	< 6	
D-7	0.3	1400	80	NH_4NO_3 + MORB	Graphite-lined $Pt_{95}Rh_{05}$	2.00	2.00	silicate	n.d.		n.d.		Ab.		63	1	Ab.		n.d.		n.d.	
D-8	0.3	1400	60	Fe_7N_3 + 5%Si + MORB	Graphite-lined $Pt_{95}Rh_{05}$	−2.53	−1.96	Metal + silicate	0.09	0.01	25	3	4.41	0.47	318	21	0.09	0.05	1757	281	3	2
D-9	0.3	1400	80	Fe_7N_3 + 1.5%Si + MORB	Graphite-lined $Pt_{95}Rh_{05}$	−1.84	−1.25	Metal + silicate	0.11	0.00	38	0	4.52	0.41	130	14	0.09	0.04	1205	111	7	3
D-10	0.3	1400	70	Fe_7N_3 + 1.5%Si + MORB	Graphite-lined $Pt_{95}Rh_{05}$	−2.01	−1.47	Metal + silicate	0.06	0.00	31	1	4.10	0.73	170	3	0.16	0.05	1333	241	9	3
D-11	0.3	1400	70	Fe_7N_3 + Si_3N_4 + MORB	Graphite-lined $Pt_{95}Rh_{05}$	−2.57	-1.99	Metal + silicate	0.05	0.00	19	2	4.50	0.45	279	26	0.11	0.04	2328	368	4	2

[a] The added Si or Ni (in wt%) is relative to the Fe in Fe_7N_3. MORB: mid-ocean ridge basalt; NWA: olivine-phyric shergottite, which represents Martian mantle-derived basalt; LTB: low TiO_2 lunar basalt.
Note that Fe_7N_3 and silicate were added in the graphite-lined $Pt_{95}Rh_{05}$ capsules in a mass proportion of ~1: 1, and the experiments were saturated with both graphite and N_2-rich gas.
[b] Ideal fO_2;
[c] Non-ideal fO_2. See text for the estimation of sample fO_2.
[d] Metal and silicate refer to the metallic melt and silicate melt, respectively.
n.d.: not determined; Ab.: absence of a metal phase; 1-σ is one sigma standard deviation based on replicate analyses.

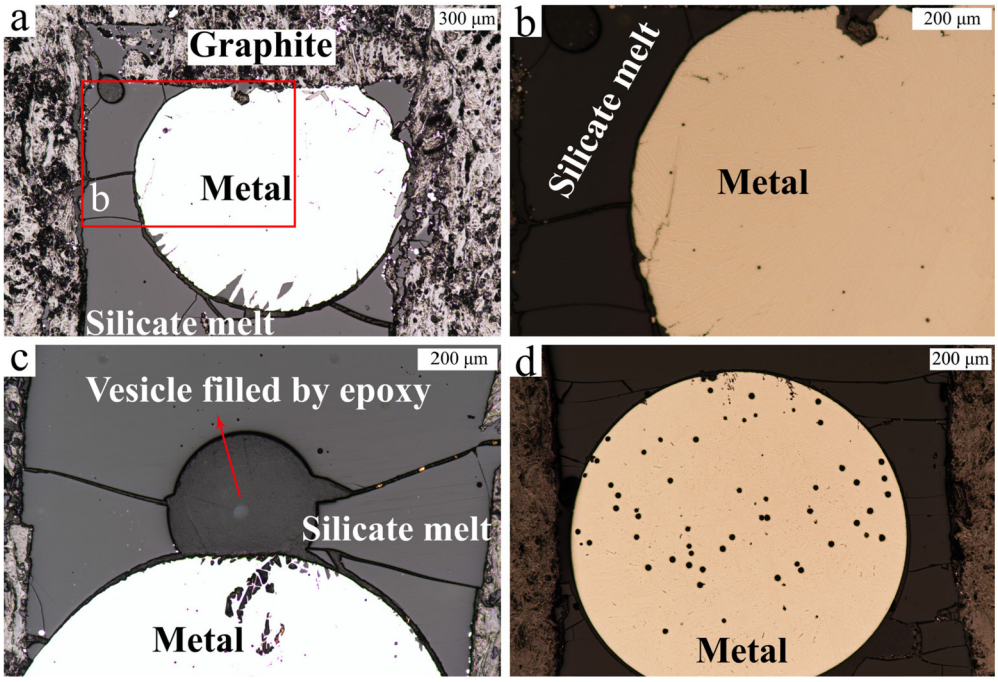

Fig. 1. Reflected-light photomicrographs of typical run products synthesized in graphite-lined $Pt_{95}Rh_{05}$ capsules. (**a**) Run D-10 (0.3 GPa and 1400 °C) shows the coexistence of metallic melt, silicate melt, and a small vesicle filled by epoxy. (**b**) Close-up view of the metallic melt in (**a**). (**c**) Run D-09 (0.3 GPa and 1400 °C) shows the coexistence of metallic melt, silicate melt, and a large vesicle filled by epoxy. (**d**) Run NS-12 (1 GPa and 1400 °C) shows a big metallic sphere surrounded by silicate melt, which in turn contains a number of small vesicles. Note that the presence of vesicles confirms that the experiments were saturated with N_2-rich gas.

fO_2 (Fig. 3a, b). Both $S_N^{silicate}$ and $S_C^{silicate}$ increase with increasing pressure and temperature (Fig. 3c, d). The $S_C^{silicate}/S_N^{silicate}$ is a strong function of fO_2, which is as high as 2 at fO_2 > IW-0.5 but below 0.01 at fO_2 < IW-3 (Fig. 3e). The $S_C^{silicate}$ values reported here are consistently larger than previous values obtained in N-free systems investigated at similar P–T–fO_2 conditions, whereas our results agree with the values previously obtained for N-bearing systems (Fig. 3b–d). The positive effect of temperature on both $S_N^{silicate}$ and $S_C^{silicate}$, and the positive effect of pressure on $S_N^{silicate}$ are consistent with previous observations (Bernadou et al., 2021; Chi et al., 2014; Dasgupta et al., 2013, 2022). However, the weak but positive effect of pressure on $S_C^{silicate}$ contrasts with previous experimental results that showed a negative effect of pressure in N-free systems (Dasgupta et al., 2013; Li et al., 2017). The explanation for the difference is that the presence of N enhances $S_C^{silicate}$ as both mentioned above and observed in Fig. 3b.

We used the most recent N-solubility model (Dasgupta et al., 2022), which takes the effects of both fO_2 and the silicate melt composition into account, to predict $S_N^{silicate}$ of our experiments. The results show that the predicted $S_N^{silicate}$ values are consistent with our measured values when our silicate melts contain more than 1 wt% TiO_2; however, the predicted values would be significantly larger than our measured values when the silicate melts contain less than 1 wt% TiO_2 (Fig. S2). The effect of TiO_2 on $S_N^{silicate}$ for reduced silicate melts appears to be overestimated in the N-solubility model. We find that the variations of both our $S_N^{silicate}$ and $S_C^{silicate}$ (Fig. 3a-d) can well be explained by the variations of our experimental parameters:

$$\log(S_N^{silicate},\ \text{ppm}) = 3.25(1.32) - 2504(2014)/\text{T} + 576(105)\text{P/T} - 0.34(0.17)\text{NBO/T} - 0.44(0.07)\Delta\text{IW} - 92(30)$$

$$\log(1 - C_{H_2O}^{silicate},\ \text{wt\%})(\text{IW-4} < fO_2 < \text{IW} + 0.4;\ R^2 = 0.88) \quad (3)$$

$$\log(S_C^{silicate},\ \text{ppm}) = 4.82(0.67) - 5392(989)/\text{T} + 254(53)\text{P/T} + 0.15(0.09)\text{NBO/T} + 0.20(0.04)\Delta\text{IW-76}(16)$$

$$\log(1 - C_{H_2O}^{silicate},\ \text{wt\%})(\text{IW-2} < fO_2 < \text{IW} + 0.4;\ R^2 = 0.96) \quad (4)$$

where T is temperature in K, P is pressure in GPa, and ΔIW is fO_2 relative to the IW buffer, $C_{H_2O}^{silicate}$ is the water content in silicate melt in wt%, and numbers in parentheses are 1σ uncertainties. We further find that the variations of our $S_C^{silicate}/S_N^{silicate}$ (Fig. 3e) can also be explained by the equation:

$$\log(S_C^{silicate}/S_N^{silicate}) = 1.13(1.05) - 2577(1575)/\text{T} - 264(81)\text{P/T} + 0.56(0.13)\text{NBO/T} + 0.51(0.05)\Delta\text{IW}(\text{IW-4} < fO_2 < \text{IW} + 0.4;\ R^2 = 0.94) \quad (5)$$

Eq. (5) implies that fO_2, P–T, and silicate melt composition all can affect $S_C^{silicate}/S_N^{silicate}$; decreasing pressure, increasing temperature, and increasing fO_2 and NBO/T all would result in an increase in $S_C^{silicate}/S_N^{silicate}$.

3.3. The N–C–H–O speciation in silicate melts

Typical Raman spectra collected from our silicate glasses are shown in Fig. 4. The peaks at ~2900 cm^{-1} are due to the presence of C–H species, and the peaks at ~3280 cm^{-1} have been assigned to NH_3/N–H species (Armstrong et al., 2015; Dalou et al., 2019; Grewal et al., 2020; Li et al., 2015a, 2016a). Increasing pressure and/or decreasing fO_2 enhance the intensity of the ~3280 cm^{-1} peak (Fig. 4). The ~2120 cm^{-1} peak was assigned to different C species: iron-carbonyl (Wetzel et al., 2013), C≡O (Stanley et al., 2014; Yoshioka et al., 2015), and CN^- (Grewal et al., 2020, 2019b). Dalou et al. (2019) determined that the ~2120 cm^{-1} peak area increases with both increasing fCO and fO_2, which strongly supports the ~2120 cm^{-1} peak as C≡O. Here we find that increasing P–T favors the presence of, and enhances the intensity of, the ~2120 cm^{-1} peak. Decreasing fO_2 appears to favor the presence of the ~2120 cm^{-1} peak for samples synthesized at 0.3 GPa, but this effect cannot be seen in the samples synthesized at 1 GPa. The ~2120 cm^{-1} peak was observed in FeO-free and

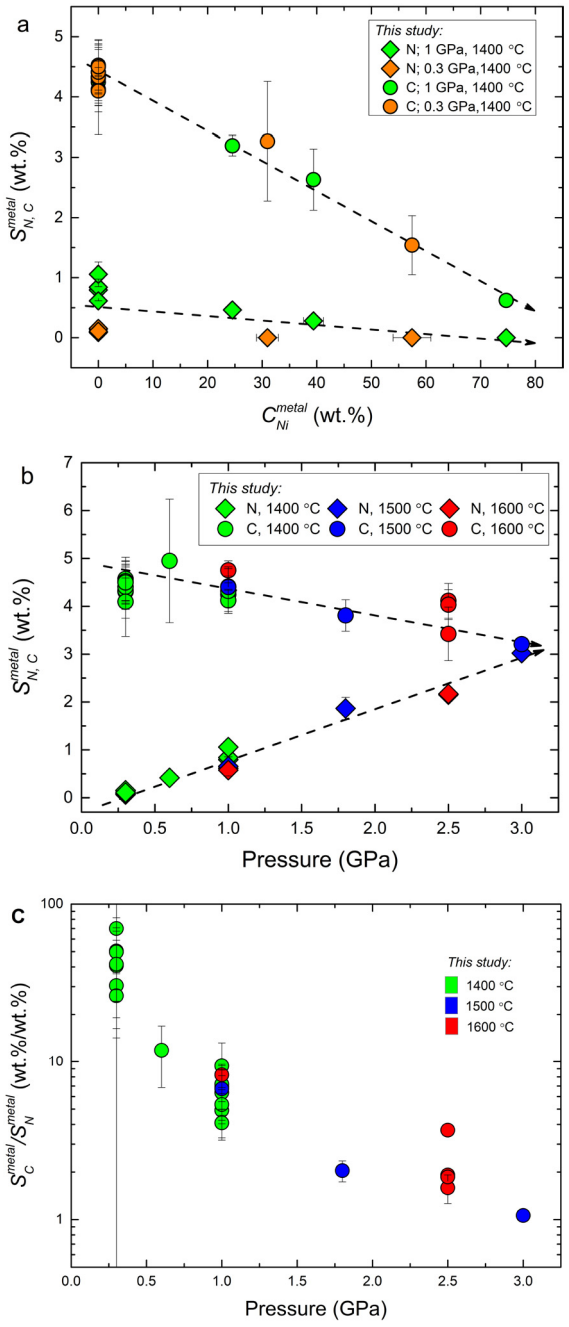

Fig. 2. The N and C solubility ($S^{metal}_{N,C}$ in wt%) and solubility ratio ($S^{metal}_{C}/S^{metal}_{N}$) of metallic melts at the saturation of graphite and N_2. (**a**) $S^{metal}_{N,C}$ decreases with increasing Ni content in metallic melts. (**b**) S^{metal}_{N} increases from ~0.1 to 3.0 wt% as pressure increases from 0.3 to 3 GPa, but S^{metal}_{C} decreases from ~4.9 to 3.2 wt% with increasing pressure. (**c**) $S^{metal}_{C}/S^{metal}_{N}$ decreases from ~70 to 1 as pressure increases from 0.3 to 3 GPa.

nominally N-free basalts (Yoshioka et al., 2015), so it seems unlikely that the ~2120 cm^{-1} peak is due to iron-carbonyl or CN^-. The ~2120 cm^{-1} peak was never observed in nominally N-free basalts in experiments at 1–8 GPa, 1400–2200 °C, and fO_2 of IW-5.3 to IW+1.7 (Chi et al., 2014; Dasgupta et al., 2013; Li et al., 2015a, 2017; Li et al., 2016a). Also, the ~2120 cm^{-1} peak was never observed in N- and C-bearing basalts in the experiments at 1.5–4 GPa, 1400–1550 °C, and fO_2 of IW-1.5 to IW-3.7 (Kadik et al., 2015). Thus, despite all of these observations, the species responsible for the ~2120 cm^{-1} peak and the stability field of such species as a function of P–T–fO_2 remain elusive. We note that $S^{silicate}_{C}$ is higher in N-bearing basalts than in N-free basalts as observed both by this study and as reported by Grewal et al. (2019b).

The dissolution of N in silicate melts is strongly controlled by fO_2. At fO_2 > IW, N dissolves physically as molecular N_2 (Gao et al., 2022; Li et al., 2015b; Libourel et al., 2003), while it dissolves chemically as reduced species at fO_2 < IW, such as N^{3-} and NH_3/N–H (Armstrong et al., 2015; Bernadou et al., 2021; Boulliung et al., 2020; Dalou et al., 2019; Grewal et al., 2020; Li et al., 2015b; Libourel et al., 2003). The dissolution of N as reduced species in silicate melts at N_2-saturation can be written as:

$$N_2\,(gas) + 3O^{2-}\,(silicate) = 2N^{3-}\,(silicate) + 3/2O_2\,(gas) \quad (6)$$

$$N_2\,(gas) + 3H_2\,(gas) = 2NH_3\,(silicate) \quad (7)$$

$$N_2\,(gas) + H_2\,(gas) = 2N\text{–}H\,(silicate) \quad (8)$$

$$H_2\,(gas) + 1/2O_2\,(gas) = H_2O\,(silicate) \quad (9)$$

The equilibrium constant (K) of Eq. (6) can be written as:

$$K_3 = \left[(fO_2)^{3/2}\cdot(\alpha N^{3-})^2\right]/\left[(fN_2)\cdot(\alpha O^{2-})^3\right] \quad (10)$$

Eq. (10) can be arranged as:

$$2\log(\alpha N^{3-}) = -3/2\log fO_2 + \log K_3 + 3\log(\alpha O^{2-}) + \log fN_2 \quad (11)$$

For a given silicate melt with N_2-saturation at given P–T conditions, Eq. (11) can be simplified as:

$$\log(C^{silicate}_{N^{3-}},\ ppm) = -3/4\log fO_2 + A \quad (12)$$

In Eqs. (10)–(12), α and f refer to activity and fugacity, respectively; $C^{silicate}_{N^{3-}}$ is the concentration of dissolved N^{3-} in silicate melts; and A is a constant. Similarly, when additional N dissolves as NH_3 or N–H in hydrous silicate melts at given $P-T$ conditions, the following equations can be derived from Eqs. (7)–(9):

$$\log(C^{silicate}_{NH_3},\ ppm) = 3/2\log(C^{silicate}_{H_2O},\ wt\%) - 3/4\log fO_2 + A \quad (13)$$

$$\log(C^{silicate}_{N-H},\ ppm) = 1/2\log(C^{silicate}_{H_2O},\ wt\%) - 1/4\log fO_2 + A \quad (14)$$

Eqs. (12)–(14) imply that a low fO_2 and/or a high water content in the silicate melt would favor the dissolution of N as N^{3-}, and as NH_3/N–H in the silicate melt. Eqs. (12)–(14) also imply that for a dry silicate melt, log ($S^{silicate}_{N}$, ppm) should increase with decreasing log fO_2 with a slope of −3/4; however, the slope should be more negative than −3/4 for a hydrous silicate melt that also contains NH_3 and/or N–H. Fig. 3a shows that the slopes for the dry silicate melts synthesized at 1 bar and fO_2 < IW-1.5 (Libourel et al., 2003) are −0.70 to −0.67, which are close to the theoretical value of −0.75. However, the slopes for our data obtained at 0.3 and 1 GPa are −0.47 and −0.60, respectively (Fig. 3a). The reason for these higher slope values could be due to the dissolution of a considerable amount of N_2 in the silicate melt. For the experiments at 0.3 GPa and fO_2 < IW, we corrected all $S^{silicate}_{N}$ values by subtracting the $S^{silicate}_{N}$ value obtained at fO_2 of ~IW+2. Refitting of the corrected $S^{silicate}_{N}$ values as a function of fO_2 yielded a slope of −0.92 (Fig. 3a), which is more negative than the theoretical value of −0.75, but consistent with our Raman measurements that NH_3/N–H was present in our reduced silicate melts. The theoretical considerations here suggest that N^{3-} and NH_3/N–H are the main N species dissolved in reduced silicate melts, although N^{3-} may form different N^{3-}–cation complexes, which may or may not be Raman-active.

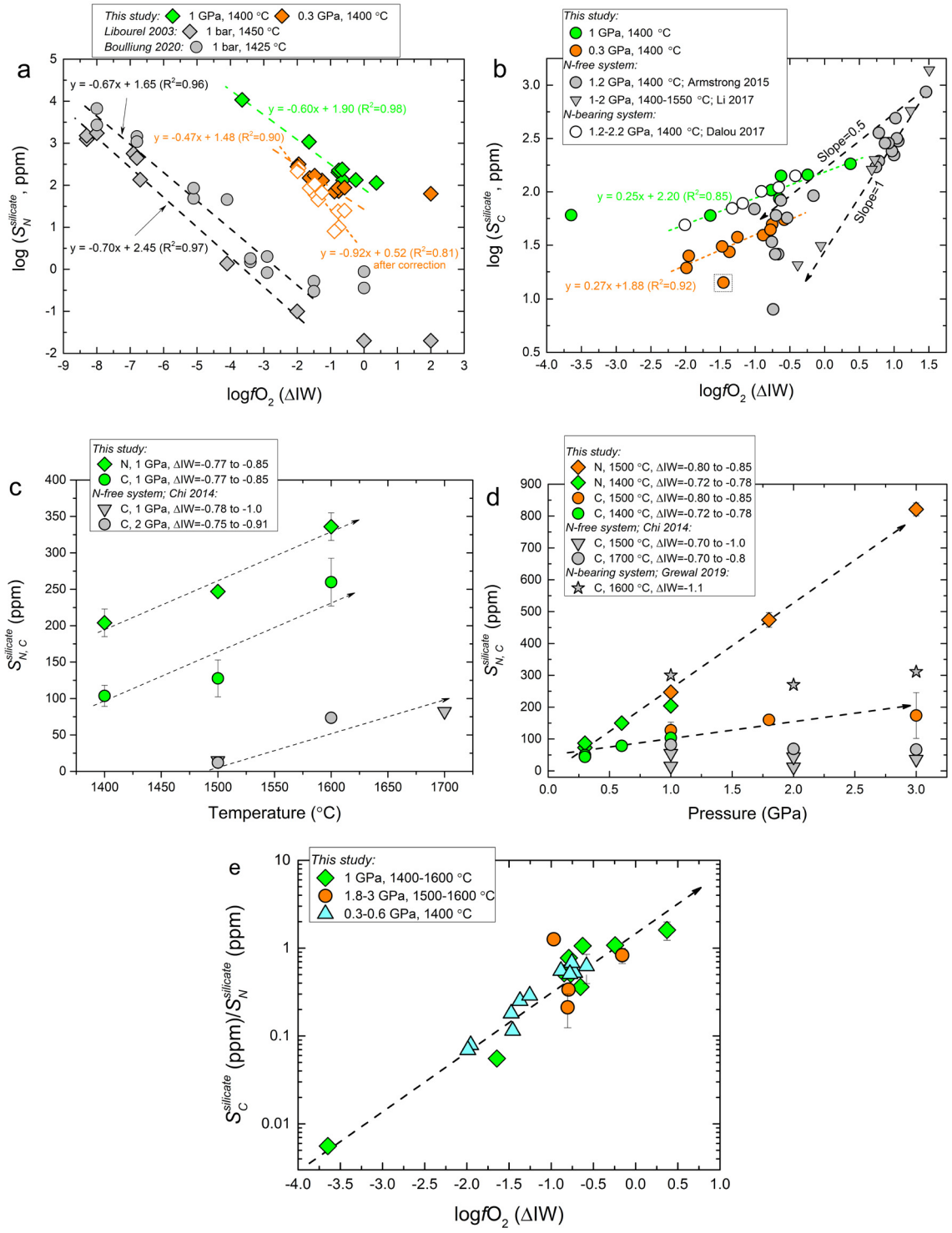

Fig. 3. The N and C solubility ($S^{silicate}_{N,C}$, in ppm) and solubility ratio ($S^{silicate}_{C}/S^{silicate}_{N}$) of silicate melts at the saturation of graphite and N_2. (**a**) $S^{silicate}_{N}$ increases with decreasing fO_2 at 0.3 and 1 GPa. Note that $C^{silicate}_{N}$ changes by some five orders of magnitude. (**b**) $S^{silicate}_{C}$ decreases with decreasing fO_2. (**c**, **d**) $C^{silicate}_{N,C}$ increases with increasing temperature and pressure. The literature data in previous studies obtained at similar $P-T-fO_2$ conditions are plotted for comparison (Armstrong et al., 2015; Boulliung et al., 2020; Chi et al., 2014; Dalou et al., 2017; Li et al., 2017; Libourel et al., 2003). (**e**) $S^{silicate}_{C}/S^{silicate}_{N}$ increases from 0.006 to 1.6, as the fO_2 increases from IW-3.7 to IW+0.4; fO_2 plays a key role in controlling $S^{silicate}_{C}/S^{silicate}_{N}$, but the effects of other parameters such as silicate melt composition and temperature, as considered in Eq. (5), cannot be neglected.

As done for N, the dissolution of C as CO_3^{2-}, C≡O, and CH_4 in silicate melts at graphite-saturation can be written as:

$$\log(C^{silicate}_{CO},\ \text{ppm}) = 1/2\log fO_2 + A \quad (15)$$

$$\log(C^{silicate}_{CO_3^{2-}},\ \text{ppm}) = \log fO_2 + A \quad (16)$$

$$\log(C^{silicate}_{CH_4},\ \text{ppm}) = 2\log(C^{silicate}_{H_2O},\ \text{wt\%}) - 3\log fO_2 + A \quad (17)$$

Eqs. (15)–(17) imply that log ($S^{silicate}_{C}$, ppm) should decrease with decreasing $1/2\log fO_2$ or $\log fO_2$ if C dissolves as CO or CO_3^{2-} in the silicate melt, respectively. However, log ($S^{silicate}_{C}$, ppm) would increase with decreasing $3\log fO_2$ and increasing water content in

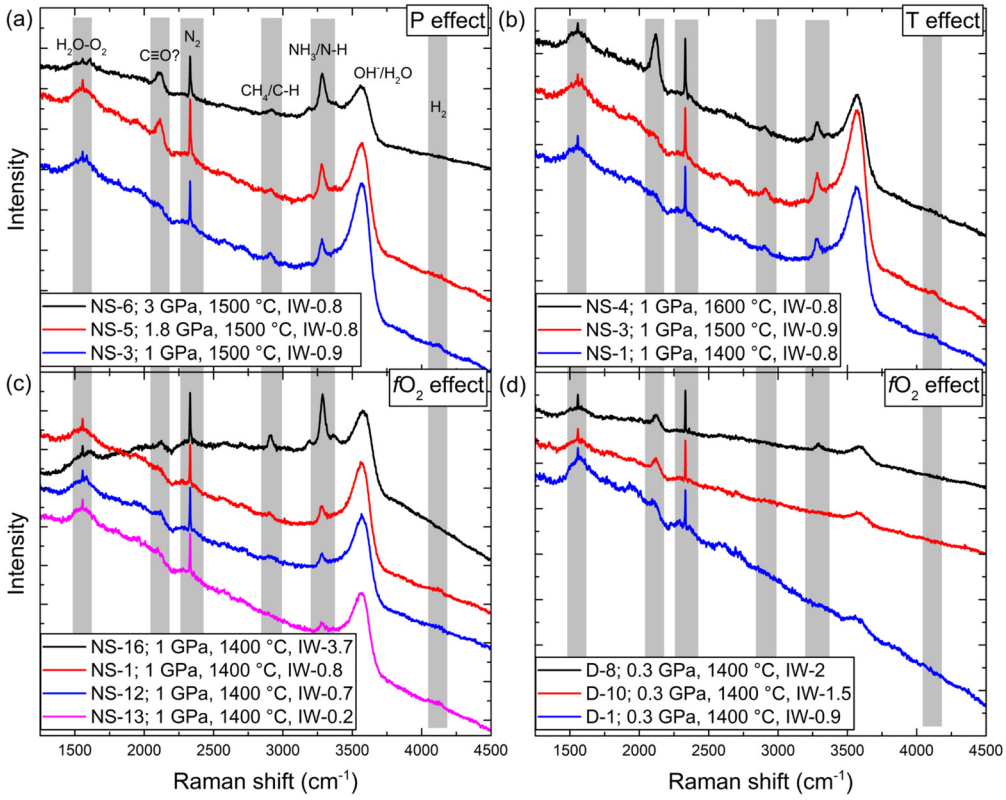

Fig. 4. Typical Raman spectra showing the N–C–H–O species dissolved in silicate melts. The peaks are assigned to be OH^-/H_2O for the broad peaks at ~3350–3650 cm^{-1} and at ~1430–1680 cm^{-1}, CH_4/C–H for the peaks at ~2900 cm^{-1}, H_2 for the peaks at ~4124 cm^{-1}, and NH_3/N–H for the peaks at ~3280 cm^{-1}, and probably C≡O for the peaks at ~2120 cm^{-1}. The peak at 1556 cm^{-1} is due to O_2 from the air, and the peak at ~2331 cm^{-1} is also in part due to N_2 from the air. The relative intensities of these peaks are shown as a function of pressure (**a**), temperature (**b**), and fO_2 (**c**, **d**). In (**c**) and (**d**) the pressure is different, 1 and 0.3 GPa, respectively. See the main text for detailed discussion.

the silicate melt if C dissolves as CH_4 in the silicate melt. Fig. 3b shows that log ($S_C^{silicate}$) of previous experiments performed at conditions similar to ours decreases with decreasing $\log fO_2$ with a slope between 0.54 and 0.95, indicating that C is dissolved mainly as CO and CO_3^{2-} in the N-free silicate melts. Our data obtained at 0.3 and 1 GPa yielded slopes of 0.27 and 0.25, respectively. These observations indicate that in addition to CO and CO_3^{2-}, other C species must also be present in our reduced silicate melts. As evidenced by the elevated $S_C^{silicate}$, new C–N species must form in N-bearing reduced silicate melts, though more sophisticated spectroscopic measurements will be required to identify the actual C–N species.

3.4. Metal/silicate partition coefficients $D_{N,C}^{metal/silicate}$

The $D_{N,\,C}^{metal/silicate}$, as calculated based on the N and C weight proportions in the metallic and silicate melts, were 1–114 and 34–3050, respectively. $D_N^{metal/silicate}$ increase with increasing fO_2 or pressure but decrease with increasing temperature (Fig. 5a–c). $D_C^{metal/silicate}$ increase with decreasing fO_2 but decrease with increasing $P-T$ (Fig. 5a–c). The $D_C^{metal/silicate}/D_N^{metal/silicate}$ ratios were 1.5–1140, which decrease with increasing pressure and/or fO_2 (Fig. 5d). These $D_N^{metal/silicate}$ and $D_C^{metal/silicate}/D_N^{metal/silicate}$ are consistent with previous results obtained from N- and C-bearing systems at similar P–T–fO_2 conditions, but the present $D_C^{metal/silicate}$ are generally lower than previously published results obtained from N-free systems (Fig. 5). We believe that the lower $D_C^{metal/silicate}$ obtained from N-bearing systems is caused by the higher $S_C^{silicate}$ but lower S_C^{metal} in N-bearing systems as compared to N-free systems. The factors that affect $S_{N,\,C}^{silicate}$ and $S_{N,C}^{metal}$ must affect $D_{N,C}^{metal/silicate}$ and thus $D_C^{metal/silicate}/D_N^{metal/silicate}$. The $D_C^{metal/silicate}/D_N^{metal/silicate}$ ratios in this study were 1.5–1140 at IW-4 $< fO_2 <$ IW, which can be described best by the following equation:

$$\log(D_C^{metal/silicate}/D_N^{metal/silicate}) = 2.4(0.2) - 691(84)\mathrm{P/T} - 0.78(0.19)\mathrm{NBO/T} - 0.53(0.07)\Delta\mathrm{IW} + 177(26)\log(1 - C_{H_2O}^{silicate},\ \mathrm{wt\%}) - 1.4(0.5)\log(1 - C_{\mathrm{Ni}}^{metal},\ \mathrm{wt\%}) \quad (\mathrm{IW\text{-}4} < fO_2 < \mathrm{IW};\ R^2 = 0.98) \quad (18)$$

Eq. (18) implies that $D_C^{metal/silicate}/D_N^{metal/silicate}$ decreases with increasing pressure, fO_2, the water content in silicate melts, and/or the silicate melt NBO/T. As shown in Fig. 5, however, it may be interesting to perform experiments at pressures higher than 3 GPa and probably at higher fO_2 to investigate whether N can become more siderophile than C when the system is saturated with graphite and N_2-rich gas, although previous studies show that $D_C^{metal/silicate}$ are overall larger than $D_N^{metal/silicate}$ at pressures as high as 26 GPa (Blanchard et al., 2022; Dalou et al., 2017; Grewal et al., 2019b; Jackson et al., 2021; Roskosz et al., 2013).

4. Discussion

4.1. C–N fractionation during silicate MO degassing

A significant population of asteroid-sized bodies underwent melting and core–mantle differentiation in the first several million years of solar system history (Fu and Elkins-Tanton, 2014), and short-lived magma oceans may have developed on essentially all

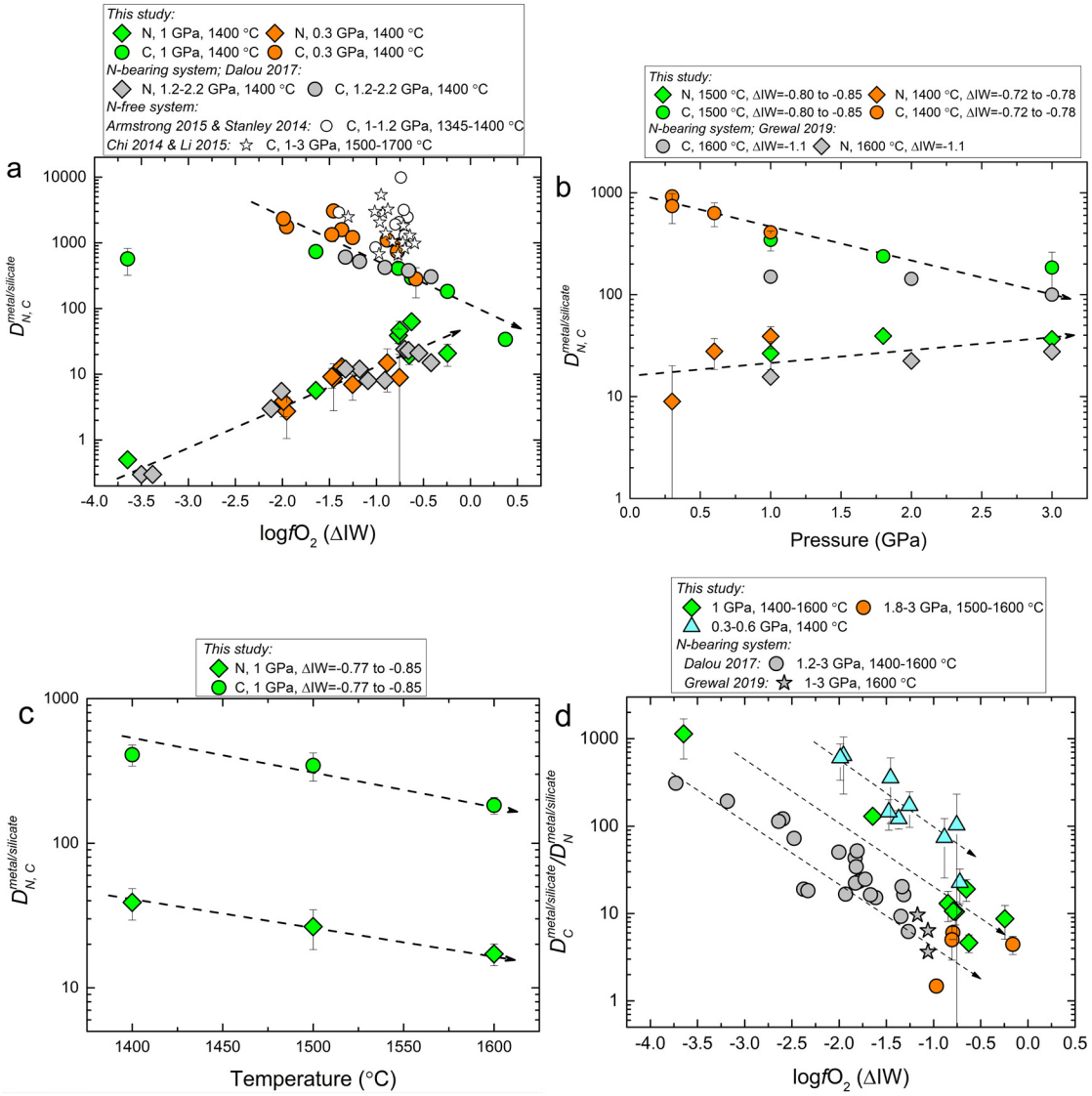

Fig. 5. The partition coefficients of N and C between the metallic and silicate melts ($D_{N,C}^{metal/silicate}$) and the $D_C^{metal/silicate}/D_N^{metal/silicate}$ ratios. (**a**) $D_N^{metal/silicate}$ increase from ~0.5 to 65 with increasing fO_2 at 0.3 and 1 GPa, while $D_C^{metal/silicate}$ decrease from 3000 to 30 with increasing fO_2. (**b**) $D_N^{metal/silicate}$ increase with increasing pressure but the $D_C^{metal/silicate}$ decrease with increasing pressure. (**c**) $D_{N,C}^{metal/silicate}$ decrease with increasing temperature. (**d**) $D_C^{metal/silicate}/D_N^{metal/silicate}$ decreases with increasing of both fO_2 and pressure. The literature data in previous studies obtained at similar P–T–fO_2 conditions are plotted for comparison (Armstrong et al., 2015; Chi et al., 2014; Dalou et al., 2017; Grewal et al., 2019b; Li et al., 2015a; Stanley et al., 2014).

planetesimals of sufficient mass (Greenwood et al., 2005; Young et al., 2019). Volatile ratios and isotope signatures indicate that planetary rocky bodies rapidly became depleted in volatiles following extensive melting and differentiation and impactor collisions, as pyroclastic eruptions, degassing or evaporation of silicate MOs, and crustal erosions all result in volatile losses (Collinet and Grove, 2020; Pringle and Moynier, 2017; Sarafian et al., 2017; Young et al., 2019). The fO_2-dependence of $S_C^{silicate}/S_N^{silicate}$ implies that degassing must cause C–N fractionation in silicate MOs (Gaillard et al., 2022), because the fO_2 of planetary rocky bodies spans more than eight log units (Boujibar et al., 2020). The core–mantle equilibrium fO_2 ranged from ~IW-6 to IW-3 for the MOs of both Mercury and the aubrite parent body (AuPB), ~IW-1.5 to IW-0.5 for the MO of Vesta, ~IW-2 for the MO of Earth's Moon, and above IW for the MOs of S-rich bodies of chondritic bulk compositions (Bercovici et al., 2022; Boujibar et al., 2020). The core–mantle equilibrium fO_2 of Earth's MO may have evolved from ~IW-5 to IW-1.5 from early to late accretion stages (Rubie et al., 2015). However, for proto-planets that had MO depths larger than 15–20 GPa, the surface MO could have become self-oxidized, with fO_2 a few log units higher than the core–mantle equilibrium fO_2. This is because the deep MO was rich in Fe^{3+}, and magmatic transportation of Fe^{3+} to the shallow MO through convection could cause oxidization (Armstrong et al., 2019; Deng et al., 2020). For example, the fO_2 of Earth's surface MO could have been between IW+1 and IW+4 when the Earth's MO depth was at 25–90 GPa (Armstrong et al., 2019; Deng et al., 2020). Therefore, a bulk reduced MO may have had an oxidized surface, where degassing of the silicate MO took place.

We have calculated the solubility-controlled C/N ratio in silicate MOs as a function of N loss fraction during degassing at variable fO_2 values using a CI chondrite-like initial C/N ratio of 20 (Hirschmann, 2016). During the degassing of silicate MOs, open-system fractionation of N and C may take place, for which we assumed a Rayleigh distillation process:

$$(C/N)_{resid} = (C/N)_{init} \times f_N^{[(K_N/K_C)-1]} \quad (19)$$

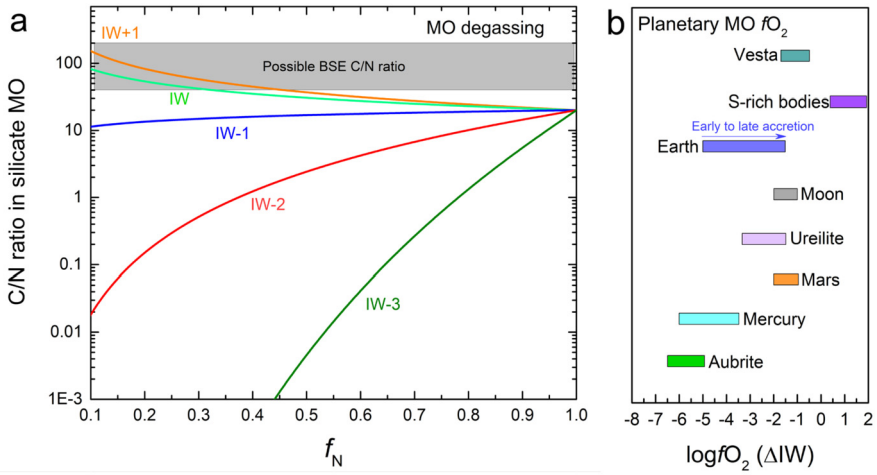

Fig. 6. C/N ratio in a silicate magma ocean (MO) as a function of the fraction of N remaining in the silicate MO (f_N) and fO_2 during degassing. (**a**) Note that the degassing conditions were fixed at 1400 °C, 0.1 GPa, and silicate melt NBO/T = 1.5, and the fO_2 was varied from IW-3 to IW+1 to cover planetary MO oxidation states. The range of possible BSE C/N ratio was constrained using the data from Hirschmann (2016) and Marty et al. (2020). (**b**) The core–mantle equilibrium fO_2 of planetary rocky bodies span about eight log units; the fO_2 values were taken from previous studies (Bercovici et al., 2022; Boujibar et al., 2020; Rubie et al., 2015).

where $(C/N)_{init}$ and $(C/N)_{resid}$ refer to the C/N ratio of the silicate MO before and after degassing, respectively; f_N is the fraction of N retained in the silicate MO after degassing; and K_i is the solubility coefficient (Henry's law constant). To model C–N fractionation in silicate MOs, the K_N/K_C, which equals $S_C^{silicate}/S_N^{silicate}$, was calculated using Eq. (5) at 1400 °C, 0.001 to 0.1 GPa, and NBO/T = 1.5. The results of this modeling are shown in Fig. 6a, with fO_2 of planetary MOs plotted in Fig. 6b. We noticed that varying the P–T–NBO/T conditions for a degassing MO does not change considerably the results shown in Fig. 6a, because the fO_2 dominates the determination of K_N/K_C. Fig. 6a shows that the C/N ratio in silicate MOs varies from <0.01 at fO_2 < IW-2 to >250 at fO_2 > IW; a C/N ratio of ~20 was obtained only when the fO_2 is between IW-1 and IW. Fig. 6a illustrates that C–N fractionation can be significant during silicate MO degassing. Degassing of the lunar or Martian silicate MO could have decreased the C/N ratio in the silicate MO; whereas, degassing of the MO of a S-rich and oxidized body should have led to an increase in the C/N ratio in the silicate MO. The degassing of Earth's reduced silicate MO during Earth's early accretion stages, when the fO_2 of surface MO was below IW-1.5, could have decreased the C/N ratio in the silicate MO, and the C/N ratio should have been higher in the atmosphere than in the silicate MO. However, for a growing Earth with MO depth larger than ~15–20 GPa, the surface MO could have become self-oxidized, with fO_2 above IW. In this circumstance, degassing should have led to an increase in the C/N ratio in the silicate MO and a low C/N ratio in the atmosphere.

4.2. C–N fractionation during planetary core–mantle segregation

The fO_2-dependence of $D_C^{metal/silicate}/D_N^{metal/silicate}$ (Fig. 5d) and the large fO_2 variations seen in planetary MOs (Fig. 6b) imply that core-formation must have also caused C–N fractionation in the spectrum of silicate MOs. $D_C^{metal/silicate}$ are higher than $D_N^{metal/silicate}$ under both presently and the previously investigated conditions (Fig. 5), indicating that C is more siderophile than N, although the determination of $D_N^{metal/silicate}$ at conditions more relevant for Earth's deep MO is still needed. Hence, if the distribution of C and N between planetary core and mantle is controlled solely by $D_C^{metal/silicate}$ and $D_N^{metal/silicate}$, and if a rocky body has a CI chondrite-like initial C/N ratio, the silicate mantle and core must have a subchondritic and superchondritic C/N ratio, respectively. However, highly reduced or oxidized MOs could have been saturated with graphite or diamond, as C is readily expelled from Si- or S-rich metallic melt (Grewal et al., 2019b; Li et al., 2015a, 2016a; Tsuno et al., 2018). As a result, the C/N ratio in the silicate MO could be considerably higher than constrained by $D_C^{metal/silicate}$ and $D_N^{metal/silicate}$. We have calculated the C/N ratio in silicate MOs under both highly reduced and oxidized conditions, using different initial C and N contents but a CI chondrite-like C/N ratio. We used a C-solubility of 1 wt% in Si-rich metallic melt for highly reduced conditions (Li et al., 2016a), and a C-solubility of 0.3 wt% in S-rich metallic melt for highly oxidized conditions (Tsuno et al., 2018). Fig. 7a illustrates that depending on the initial C and N abundances, C/N ratios of 1–20 can be achieved for silicate MOs when the core is saturated with graphite at highly reduced conditions. However, it should be noted that in this case, most C in the silicate MO is present as graphite. Likewise, degassing would result in an increase in the C/N ratio in the silicate MO, because graphite can survive degassing, as implied by both the observed graphite-flotation on Mercury's surface (Peplowski et al., 2016) and the presence of graphite in ureilite meteorites (Barrat et al., 2017). Assuming 90% of the N in the silicate MOs after core-segregation degassed into the atmosphere, the C/N ratios in the silicate MOs can be enhanced to ~10–200. Fig. 7b illustrates that C/N ratios of 20–100 can be achieved for silicate MOs after the segregation of a S-rich and C-saturated core. Degassing of such oxidized silicate MOs can further enhance the C/N ratios in the silicate MO due to the high $S_C^{silicate}/S_N^{silicate}$ (>1) under oxidized conditions.

The conditions required for C-saturation in MOs were broadened by a recent study (Keppler and Golabek, 2019), which suggested the saturation and flotation of graphite may have occurred extensively in planetary MOs. For example, the C-rich ureilite meteorites with superchondritic C/N ratios (Marty et al., 2020) and fO_2 between IW-3 and IW (Boujibar et al., 2020) were suggested to be the remnants of such a graphite-rich surface layer on a partially or completely molten planetesimal (Keppler and Golabek, 2019). This means that superchondritic C/N ratios can also be obtained in silicate MOs of planetesimals and embryos with intermediate fO_2 due to the preferential N degassing and loss, as in the case for the highly reduced or oxidized conditions.

4.3. Origin of the BSE's superchondritic C/N ratio

The origin of the BSE's superchondritic C/N ratio remains a topic of debate. Previous models proposed for explaining the BSE's superchondritic C/N ratio include: (1) preferential segregation of N

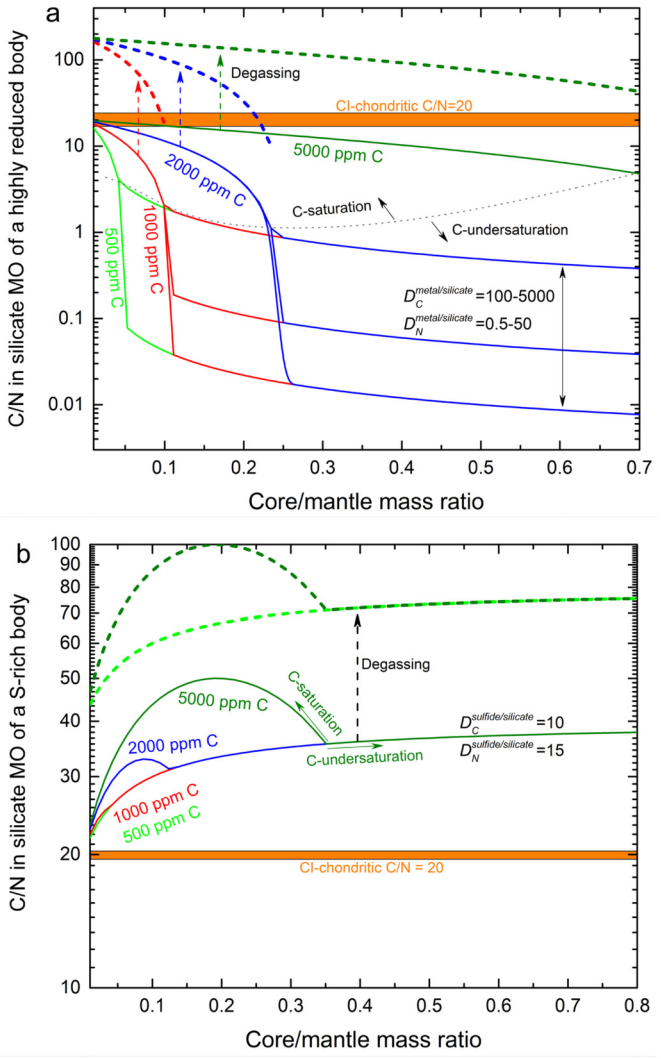

Fig. 7. C/N ratio in a silicate magma ocean (MO) defined by core–mantle segregation and degassing. (**a**) C/N ratio in the silicate MO of a highly reduced planetesimal/embryo. The C solubility in the core at highly reduced conditions was fixed at 1 wt%. Core–mantle segregation results in subchondritic C/N in the silicate MO; however, preferential N degassing ($f_N = 0.1$) at graphite-saturation leads to a superchondritic C/N ratio, as indicated by the colored arrows. The dotted gray curve separates graphite-saturation from undersaturation conditions in the core. For the calculation of C distribution between core and mantle at C-undersaturation, we used $D_C^{metal/silicate}$ of 100–5000 and $D_N^{metal/silicate}$ of 0.5–50. (**b**) C/N ratio in the silicate MO of a S-rich, oxidized planetesimal/embryo. The C solubility in the S-rich core (30 wt% S) was fixed at 1.5 wt%. The $D^{sulfide/silicate}$ for C and N were taken from Grewal et al. (2019b). Because of $D_C^{sulfide/silicate} < D_N^{sulfide/silicate}$, core–mantle segregation results in a superchondritic C/N in the silicate MO; however, preferential N degassing ($f_N = 0.5$) under oxidized conditions further enhances C/N ratio in the silicate MO, as indicated by the dashed black arrow. The f_N refers to the fraction of N remaining in the silicate MO during degassing.

into Earth's core (Marty, 2012); (2) deep storage of N in mantle minerals (Li et al., 2013); (3) Earth's atmospheric loss (Hirschmann, 2016); (4) addition of a C-rich late veneer to the proto-Earth (Dalou et al., 2017); (5) loss of immiscible N_2 from metallic melt in Earth's MO (Liu et al., 2019); (6) delivery of C and N by a S-rich giant impactor (Dasgupta and Grewal, 2019; Grewal et al., 2019b); Earth's accretion of precursors with superchondritic C/N ratios (Marty et al., 2020); and complex interplay between core segregation, volatile delivery, mantle degassing, and atmospheric loss during Earth's main accretion phase (Chen and Jacobson, 2022; Shi et al., 2022). However, the larger $D_C^{metal/silicate}$ than $D_N^{metal/silicate}$ over a large range of experimental conditions excludes core formation as a solution to the BSE's superchondritic C/N ratio (Dalou et al., 2017; Grewal et al., 2019b; Hirschmann, 2016). Storage of N in Earth's deep reduced mantle requires inhomogeneous distribution of N in Earth's mantle, which awaits future test. Earth's atmospheric loss, with or without the combination with core formation, was rejected by Dalou et al. (2017) based on the assumption that Earth's atmosphere formed above a reduced MO. Immiscibility between N_2 and Fe–N metallic melt in Earth's MO requires a few wt% N in the materials accreted to the proto-Earth, which is unrealistically high compared to the N concentrations in both chondrites and achondrites.

Processes operating on planetesimals, embryos, and accreting planets, such as core–mantle–atmosphere differentiation and subsequent impact erosion of the atmospheric and/or silicate portions, would affect the volatile budget and ratios in the finally formed protoplanets. Fig. 8 illustrates that MOs produced compositionally layered planetesimals and embryos, and the modification of such rocky bodies before and during their accretion into the proto-Earth may explain the BSE's superchondritic C/N ratio, as explained below.

(**a**) The larger $D_C^{metal/silicate}$ than $D_N^{metal/silicate}$ implies that the cores of rocky bodies have superchondritic C/N ratios if they are S- and Si-poor. Volatile loss from the silicate mantles of rocky bodies could occur during MO crystallization because of the incompatibility of both N and C in silicate minerals (Dasgupta et al., 2022; Li et al., 2013; Shcheka et al., 2006). We also assumed that the atmosphere formed by degassing was lost into the vacuum space before collision into large embryos and protoplanets. In addition, the stripping of crustal and mantle materials during collision into large embryos and protoplanets would also cause the loss of N and C into the vacuum space. Therefore, the cores of rocky bodies, with superchondritic C/N ratios, could be an important source of N and C delivered to the protoplanets (Grewal et al., 2021b). Accordingly, Earth's accretion of such rock bodies with their cores in equilibrium with Earth's silicate MO could have potentially established a superchondritic C/N ratio in the BSE, in particular if the partitioning of C into Earth's core becomes weak as the temperature and pressure increased during Earth's accretion (Blanchard et al., 2022).

(**b**) During Earth's late accretion when the cores of impacting embryos were largely in disequilibrium with Earth's silicate MO, a superchondritic C/N ratio can also be imprinted on the BSE. As shown in Fig. 7, for an embryo whose core–mantle segregation occurred at C-saturation conditions, preferential N degassing of the silicate MO would produce a superchondritic C/N ratio in the silicate MO. Therefore, assuming the loss of the embryo's atmosphere into the vacuum space before collision, the merging of the silicate mantle of such an embryo with the proto-Earth's mantle should also have helped establish a superchondritic C/N ratio in the BSE.

(**c**) We emphasize the importance of Earth's MO degassing at oxidized conditions. When Earth's MO depth was sufficiently large (>20 GPa) such that the shallow MO was self-oxidized to above IW (Armstrong et al., 2019; Deng et al., 2020), degassing of such a shallow MO could have enhanced the C/N ratio in the silicate MO, producing N-rich atmosphere (Gao et al., 2022). Subsequent collisional erosion and the resulting significant atmospheric loss (Kegerreis et al., 2020) would have stripped off more N than C from the proto-atmosphere. Therefore, multiple episodes of MO degassing and impact-induced atmospheric loss during Earth's last few giant impacts must have helped form a superchondritic C/N ratio in the BSE. Note that during Earth's last few giant impacts, the pressures of bottom MO were already larger than 40 GPa (Rubie et al., 2015) and the fO_2 of surface MO well above IW (Armstrong et al., 2019; Deng et al., 2020).

(**d**) Finally, the oxidization of a fraction of core materials of planetesimals, which were added into the proto-Earth's mantle

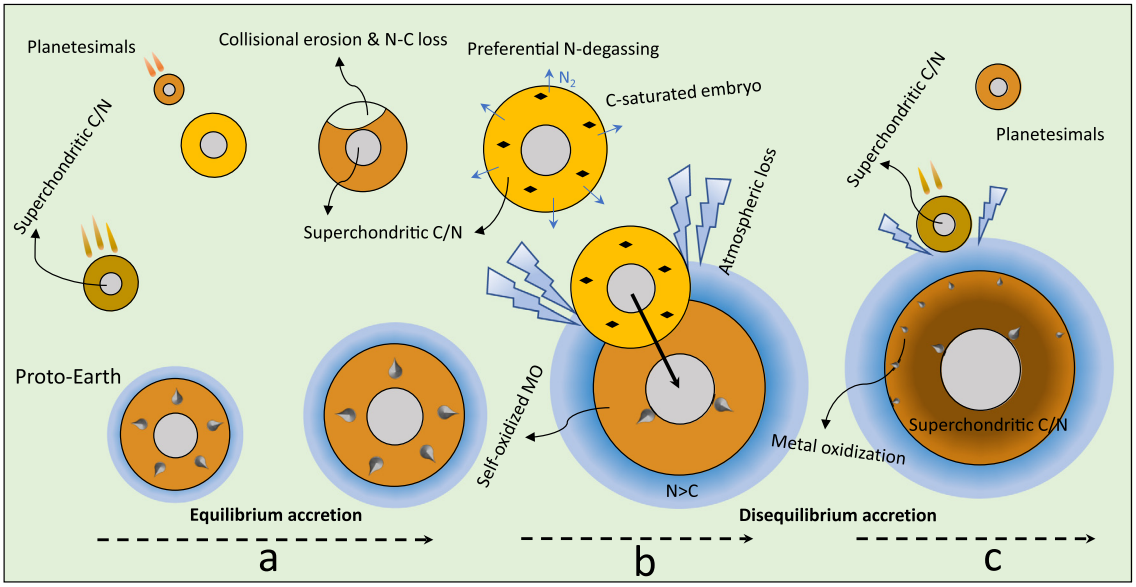

Fig. 8. Cartoon illustrating potential processes responsible for establishing the superchondritic C/N ratio in the bulk silicate Earth (BSE). (**a**) Proto-Earth accretes differentiated planetesimals and embryos with cores possessing superchondritic C/N ratios. The silicate portions of these differentiated rocky bodies may be depleted in volatiles because of silicate MO degassing and collisional erosion of mantle and crustal materials. Delivery of such rocky bodies to the proto-Earth would produce MO with a superchondritic C/N ratio. (**b**) Proto-Earth's disequilibrium accretion of C-saturated embryos with superchondritic C/N ratios in the silicate mantles, through direct core–core and mantle–mantle merging. Large proto-Earth's shallow MO was already self-oxidized, producing N-rich proto-atmosphere via degassing (as indicated by N > C). The catastrophic loss of N-rich atmosphere by collisional erosion would further increase the C/N ratio in the BSE. (**c**) During Earth's final accretion stages differentiated planetesimals were delivered to the solidifying/solidified MO, and oxidization of the emulsified cores of those planetesimals released C and N with a superchondritic C/N ratio into the BSE.

during Earth's final accretion stages (Marchi et al., 2017), should also have helped establish a superchondritic C/N ratio in the BSE. The oxidization of emulsified planetesimal cores in Earth's upper mantle seems probable, and it has been proposed to explain the relative chondritic abundance of highly siderophile elements in the BSE (Marchi et al., 2017; Sleep, 2016). This is because the transportation of Fe^{3+} from the lower mantle/deep MO into the upper mantle (Armstrong et al., 2019; Deng et al., 2020), and the hydrodynamic loss of hydrogen to space (Sleep, 2016) should have oxidized the shallow upper mantle at fO_2 around the fayalite-magnetite-quartz buffer during Earth's final accretion stages.

In summary, the origin of the BSE's superchondritic C/N ratio could be an outcome of combined processes, including core–mantle–atmosphere differentiation in planetesimals and embryos and Earth's violent accretion of such rocky bodies. In turn, the BSE's superchondritic C/N ratio may reflect that the Earth established its N and C inventories through acquiring volatiles from the cores of rocky bodies, disequilibrium accretion of C-saturated embryos, multiple episodes of MO degassing and collision-induced atmospheric loss during Earth's accretion of the last few giant impactors, and/or oxidization of planetesimal core materials in Earth's shallow upper mantle during Earth's final accretion stages. These processes should be included in the complex model of Shi et al. (2022) and Chen and Jacobson (2022) in the following studies to better understand the origin of Earth's superchondritic C/N ratio and volatiles.

CRediT authorship contribution statement

Y.L. conceived the project and performed all experiments. M.W., B.M., G.C., Y.L., and R.D. performed sample analyses. Y.L. interpreted the data and wrote the manuscript with comments and improvements from all authors.

Declaration of competing interest

The authors declare that they have no known competing financial interests or personal relationships that could have appeared to influence the work reported in this paper.

Data availability

We have shared the data in the main text and supplementary files.

Acknowledgements

We thank Celia Dalou for providing the nitrogen reference materials for SIMS calibration, and Frédéric Couffignal for assistance with the SIMS measurements at GFZ, Potsdam. Y. Li appreciates the helpful discussion with Hans Keppler. Constructive comments from Julien Boulliung, Bernard Marty, and editor Frédéric Moynier helped greatly to improve the quality of this paper. This project received support from ZDBS-LY-DQC013 and NFSC (41673064) to Y. Li. R.D. acknowledges support from NASA grants 80NSSC18K0828 and 80NSSC18K1314.

Appendix A. Supplementary material

Supplementary material related to this article can be found online at https://doi.org/10.1016/j.epsl.2023.118032.

References

Albarede, F., 2009. Volatile accretion history of the terrestrial planets and dynamic implications. Nature 461, 1227–1233.

Armstrong, K., Frost, D.J., McCammon, C.A., Rubie, D.C., Boffa Ballaran, T., 2019. Deep magma ocean formation set the oxidation state of Earth's mantle. Science 365, 903–906.

Armstrong, L.S., Hirschmann, M.M., Stanley, B.D., Falksen, E.G., Jacobsen, S.D., 2015. Speciation and solubility of reduced C–O–H–N volatiles in mafic melt: implications for volcanism, atmospheric evolution, and deep volatile cycles in the terrestrial planets. Geochim. Cosmochim. Acta 171, 283–302.

Barrat, J.-A., Sansjofre, P., Yamaguchi, A., Greenwood, R.C., Gillet, P., 2017. Carbon isotopic variation in ureilites: evidence for an early, volatile-rich Inner Solar System. Earth Planet. Sci. Lett. 478, 143–149.
Bercovici, H.L., Elkins-Tanton, L.T., O'Rourke, J.G., Schaefer, L., 2022. The effects of bulk composition on planetesimal core sulfur content and size. Icarus 380.
Bernadou, F., Gaillard, F., Füri, E., Marrocchi, Y., Slodczyk, A., 2021. Nitrogen solubility in basaltic silicate melt - implications for degassing processes. Chem. Geol. 573.
Blanchard, I., Rubie, D.C., Jennings, E.S., Franchi, I.A., Zhao, X., Petitgirard, S., Miyajima, N., Jacobson, S.A., Morbidelli, A., 2022. The metal–silicate partitioning of carbon during Earth's accretion and its distribution in the early solar system. Earth Planet. Sci. Lett. 580.
Boujibar, A., Herd, C.D.K., Righter, K., 2020. Redox processes in early Earth accretion and in terrestrial bodies. Elements 16, 161–166.
Boulliung, J., Füri, E., Dalou, C., Tissandier, L., Zimmermann, L., Marrocchi, Y., 2020. Oxygen fugacity and melt composition controls on nitrogen solubility in silicate melts. Geochim. Cosmochim. Acta 284, 120–133.
Budde, G., Burkhardt, C., Kleine, T., 2019. Molybdenum isotopic evidence for the late accretion of outer Solar System material to Earth. Nat. Astron. 3, 736–741.
Chen, H., Jacobson, S.A., 2022. Impact induced atmosphere-mantle exchange sets the volatile elemental ratios on primitive Earths. Earth Planet. Sci. Lett. 594.
Chi, H., Dasgupta, R., Duncan, M.S., Shimizu, N., 2014. Partitioning of carbon between Fe-rich alloy melt and silicate melt in a magma ocean – implications for the abundance and origin of volatiles in Earth, Mars, and the Moon. Geochim. Cosmochim. Acta 139, 447–471.
Collinet, M., Grove, T.L., 2020. Formation of primitive achondrites by partial melting of alkali-undepleted planetesimals in the inner solar system. Geochim. Cosmochim. Acta 277, 358–376.
Dalou, C., Hirschmann, M.M., von der Handt, A., Mosenfelder, J., Armstrong, L.S., 2017. Nitrogen and carbon fractionation during core–mantle differentiation at shallow depth. Earth Planet. Sci. Lett. 458, 141–151.
Dalou, C., Hirschmann, M.M., Jacobsen, S.D., Le Losq, C., 2019. Raman spectroscopy study of C-O-H-N speciation in reduced basaltic glasses: implications for reduced planetary mantles. Geochim. Cosmochim. Acta 265, 32–47.
Dasgupta, R., Grewal, D.S., 2019. Origin and early differentiation of carbon and associated life-essential volatile elements on Earth. In: Orcutt, B.N., Daniel, I., Dasgupta, R. (Eds.), Deep Carbon: Past to Present. Cambridge University Press, Cambridge, pp. 4–39.
Dasgupta, R., Chi, H., Shimizu, N., Buono, A.S., Walker, D., 2013. Carbon solution and partitioning between metallic and silicate melts in a shallow magma ocean: implications for the origin and distribution of terrestrial carbon. Geochim. Cosmochim. Acta 102, 191–212.
Dasgupta, R., Falksen, E., Pal, A., Sun, C., 2022. The fate of nitrogen during parent body partial melting and accretion of the inner solar system bodies at reducing conditions. Geochim. Cosmochim. Acta 336, 291–307.
Deng, J., Du, Z., Karki, B.B., Ghosh, D.B., Lee, K.K.M., 2020. A magma ocean origin to divergent redox evolutions of rocky planetary bodies and early atmospheres. Nat. Commun. 11, 2007.
Duncan, M.S., Dasgupta, R., Tsuno, K., 2017. Experimental determination of CO2 content at graphite saturation along a natural basalt-peridotite melt join: implications for the fate of carbon in terrestrial magma oceans. Earth Planet. Sci. Lett. 466, 115–128.
Elkins-Tanton, L.T., 2012. Magma oceans in the Inner Solar System. Annu. Rev. Earth Planet. Sci. 40, 113–139.
Fichtner, C.E., Schmidt, M.W., Liebske, C., Bouvier, A.-S., Baumgartner, L.P., 2021. Carbon partitioning between metal and silicate melts during Earth accretion. Earth Planet. Sci. Lett. 554.
Fischer, R.A., Cottrell, E., Hauri, E., Lee, K.K.M., Le Voyer, M., 2020. The carbon content of Earth and its core. Proc. Natl. Acad. Sci. 117, 8743–8749.
Fischer-Godde, M., Kleine, T., 2017. Ruthenium isotopic evidence for an inner Solar System origin of the late veneer. Nature 541, 525–527.
Fu, R.R., Elkins-Tanton, L.T., 2014. The fate of magmas in planetesimals and the retention of primitive chondritic crusts. Earth Planet. Sci. Lett. 390, 128–137.
Füri, E., Deloule, E., Dalou, C., 2018. Nitrogen abundance and isotope analysis of silicate glasses by secondary ionization mass spectrometry. Chem. Geol. 493, 327–337.
Gaillard, F., Bernadou, F., Roskosz, M., Bouhifd, M.A., Marrocchi, Y., Iacono-Marziano, G., Moreira, M., Scaillet, B., Rogerie, G., 2022. Redox controls during magma ocean degassing. Earth Planet. Sci. Lett. 577.
Gao, Z., Yang, Y.-N., Yang, S.-Y., Li, Y., 2022. Experimental determination of N2 solubility in silicate melts and implications for N2–Ar–CO2 fractionation in magmas. Geochim. Cosmochim. Acta 326, 17–40.
Greenwood, R.C., Franchi, I.A., Jambon, A., Buchanan, P.C., 2005. Widespread magma oceans on asteroidal bodies in the early Solar System. Nature 435, 916–918.
Grewal, D.S., Dasgupta, R., Holmes, A.K., Costin, G., Li, Y., Tsuno, K., 2019a. The fate of nitrogen during core-mantle separation on Earth. Geochim. Cosmochim. Acta 251, 87–115.
Grewal, D.S., Dasgupta, R., Sun, C., Tsuno, K., Costin, G., 2019b. Delivery of carbon, nitrogen, and sulfur to the silicate Earth by a giant impact. Sci. Adv. 5, eaau3669.
Grewal, D.S., Dasgupta, R., Farnell, A., 2020. The speciation of carbon, nitrogen, and water in magma oceans and its effect on volatile partitioning between major reservoirs of the Solar System rocky bodies. Geochim. Cosmochim. Acta 280, 281–301.
Grewal, D.S., Dasgupta, R., Aithala, S., 2021a. The effect of carbon concentration on its core-mantle partitioning behavior in inner Solar System rocky bodies. Earth Planet. Sci. Lett. 571.
Grewal, D.S., Dasgupta, R., Hough, T., Farnell, A., 2021b. Rates of protoplanetary accretion and differentiation set nitrogen budget of rocky planets. Nat. Geosci. 14, 369–376.
Grewal, D.S., Seales, J.D., Dasgupta, R., 2022. Internal or external magma oceans in the earliest protoplanets – perspectives from nitrogen and carbon fractionation. Earth Planet. Sci. Lett. 598.
Hirschmann, M.M., 2016. Constraints on the early delivery and fractionation of Earth's major volatiles from C/H, C/N, and C/S ratios. Am. Mineral. 101, 540–553.
Jackson, C.R.M., Cottrell, E., Du, Z., Bennett, N.R., Fei, Y., 2021. High pressure redistribution of nitrogen and sulfur during planetary stratification. Geochem. Perspect. Lett. 18, 37–42.
Kadik, A.A., Koltashev, V.V., Kryukova, E.B., Plotnichenko, V.G., Tsekhonya, T.I., Kononkova, N.N., 2015. Solubility of nitrogen, carbon, and hydrogen in FeO–Na2O–Al2O3–SiO2 melt and liquid iron alloy: influence of oxygen fugacity. Geochem. Int. 53, 849–868.
Kegerreis, J.A., Eke, V.R., Massey, R.J., Teodoro, L.F.A., 2020. Atmospheric erosion by giant impacts onto terrestrial planets. Astrophys. J. 897.
Keppler, H., Golabek, G., 2019. Graphite floatation on a magma ocean and the fate of carbon during core formation. Geochem. Perspect. Lett., 12–17.
Keppler, H., Cialdella, L., Couffignal, F., Wiedenbeck, M., 2022. The solubility of N2 in silicate melts and nitrogen partitioning between upper mantle minerals and basalt. Contrib. Mineral. Petrol. 177.
Labidi, J., Cartigny, P., Moreira, M., 2013. Non-chondritic sulphur isotope composition of the terrestrial mantle. Nature 501, 208–211.
Li, Y., Wiedenbeck, M., Shcheka, S., Keppler, H., 2013. Nitrogen solubility in upper mantle minerals. Earth Planet. Sci. Lett. 377, 311–323.
Li, Y., Dasgupta, R., Tsuno, K., 2015a. The effects of sulfur, silicon, water, and oxygen fugacity on carbon solubility and partitioning in Fe-rich alloy and silicate melt systems at 3 GPa and 1600 °C: implications for core–mantle differentiation and degassing of magma oceans and reduced planetary mantles. Earth Planet. Sci. Lett. 415, 54–66.
Li, Y., Huang, R., Wiedenbeck, M., Keppler, H., 2015b. Nitrogen distribution between aqueous fluids and silicate melts. Earth Planet. Sci. Lett. 411, 218–228.
Li, Y., Dasgupta, R., Tsuno, K., Monteleone, B., Shimizu, N., 2016a. Carbon and sulfur budget of the silicate Earth explained by accretion of differentiated planetary embryos. Nat. Geosci. 9, 781–785.
Li, Y., Marty, B., Shcheka, S., Zimmermann, L., Keppler, H., 2016b. Nitrogen isotope fractionation during terrestrial core-mantle separation. Geochem. Perspect. Lett., 138–147.
Li, Y., Dasgupta, R., Tsuno, K., 2017. Carbon contents in reduced basalts at graphite saturation: implications for the degassing of Mars, Mercury, and the Moon. J. Geophys. Res., Planets 122, 1300–1320.
Libourel, G., Marty, B., Humbert, F., 2003. Nitrogen solubility in basaltic melt. Part I. Effect of oxygen fugacity. Geochim. Cosmochim. Acta 67, 4123–4135.
Liu, J., Dorfman, S.M., Lv, M., Li, J., Zhu, F., Kono, Y., 2019. Loss of immiscible nitrogen from metallic melt explains Earth's missing nitrogen. Geochem. Perspect. Lett., 18–22.
Malavergne, V., Bureau, H., Raepsaet, C., Gaillard, F., Poncet, M., Surblé, S., Sifré, D., Shcheka, S., Fourdrin, C., Deldicque, D., Khodja, H., 2019. Experimental constraints on the fate of H and C during planetary core-mantle differentiation. Implications for the Earth. Icarus 321, 473–485.
Marchi, S., Canup, R.M., Walker, R.J., 2017. Heterogeneous delivery of silicate and metal to the Earth by large planetesimals. Nat. Geosci.
Marty, B., 2012. The origins and concentrations of water, carbon, nitrogen and noble gases on Earth. Earth Planet. Sci. Lett. 313–314, 56–66.
Marty, B., Almayrac, M., Barry, P.H., Bekaert, D.V., Broadley, M.W., Byrne, D.J., Ballentine, C.J., Caracausi, A., 2020. An evaluation of the C/N ratio of the mantle from natural CO2-rich gas analysis: geochemical and cosmochemical implications. Earth Planet. Sci. Lett. 551.
Peplowski, P.N., Klima, R.L., Lawrence, D.J., Ernst, C.M., Denevi, B.W., Frank, E.A., Goldsten, J.O., Murchie, S.L., Nittler, L.R., Solomon, S.C., 2016. Remote sensing evidence for an ancient carbon-bearing crust on Mercury. Nat. Geosci. 9, 273–276.
Pringle, E.A., Moynier, F., 2017. Rubidium isotopic composition of the Earth, meteorites, and the Moon: evidence for the origin of volatile loss during planetary accretion. Earth Planet. Sci. Lett. 473, 62–70.
Roskosz, M., Bouhifd, M.A., Jephcoat, A.P., Marty, B., Mysen, B.O., 2013. Nitrogen solubility in molten metal and silicate at high pressure and temperature. Geochim. Cosmochim. Acta 121, 15–28.
Rubie, D.C., Jacobson, S.A., Morbidelli, A., O'Brien, D.P., Young, E.D., de Vries, J., Nimmo, F., Palme, H., Frost, D.J., 2015. Accretion and differentiation of the terrestrial planets with implications for the compositions of early-formed Solar System bodies and accretion of water. Icarus 248, 89–108.
Sarafian, A.R., John, T., Roszjar, J., Whitehouse, M.J., 2017. Chlorine and hydrogen degassing in Vesta's magma ocean. Earth Planet. Sci. Lett. 459, 311–319.

Schönbächler, M., Carlson, R., Horan, M., Mock, T., Hauri, E., 2010. Heterogeneous accretion and the moderately volatile element budget of Earth. Science 328, 884–887.
Shcheka, S.S., Wiedenbeck, M., Frost, D.J., Keppler, H., 2006. Carbon solubility in mantle minerals. Earth Planet. Sci. Lett. 245, 730–742.
Shi, L., Lu, W., Kagoshima, T., Sano, Y., Gao, Z., Du, Z., Liu, Y., Fei, Y., Li, Y., 2022. Nitrogen isotope evidence for Earth's heterogeneous accretion of volatiles. Nat. Commun. 13, 1–15.
Sleep, N.H., 2016. Asteroid bombardment and the core of Theia as possible sources for the Earth's late veneer component. Geochem. Geophys. Geosyst. 17, 2623–2642.
Speelmanns, I.M., schmidt, M.W., Liebske, C., 2018. Nitrogen solubility in core materials. Geophys. Res. Lett. 45.
Speelmanns, I.M., Schmidt, M.W., Liebske, C., 2019. The almost lithophile character of nitrogen during core formation. Earth Planet. Sci. Lett. 510, 186–197.
Stanley, B.D., Hirschmann, M.M., Withers, A.C., 2014. Solubility of COH volatiles in graphite-saturated martian basalts. Geochim. Cosmochim. Acta 129, 54–76.
Tsuno, K., Grewal, D.S., Dasgupta, R., 2018. Core-mantle fractionation of carbon in Earth and Mars: the effects of sulfur. Geochim. Cosmochim. Acta 238, 477–495.
Varas-Reus, M.I., König, S., Yierpan, A., Lorand, J.-P., Schoenberg, R., 2019. Selenium isotopes as tracers of a late volatile contribution to Earth from the outer Solar System. Nat. Geosci.
Wang, Z., Becker, H., 2013. Ratios of S, Se and Te in the silicate Earth require a volatile-rich late veneer. Nature 499, 328–331.
Wetzel, D.T., Rutherford, M.J., Jacobsen, S.D., Hauri, E.H., Saal, A.E., 2013. Degassing of reduced carbon from planetary basalts. Proc. Natl. Acad. Sci. 110, 8010–8013.
Wood, B.J., Li, J., Shahar, A., 2013. Carbon in the core: its influence on the properties of core and mantle. Rev. Mineral. Geochem. 75, 231–250.
Yoshioka, T., McCammon, C., Shcheka, S., Keppler, H., 2015. The speciation of carbon monoxide in silicate melts and glasses. Am. Mineral. 100, 1641–1644.
Young, E.D., Shahar, A., Nimmo, F., Schlichting, H.E., Schauble, E.A., Tang, H., Labidi, J., 2019. Near-equilibrium isotope fractionation during planetesimal evaporation. Icarus 323, 1–15.